

# On the Nucleosynthesis of Nitrogen

James W. Johnson,<sup>1\*</sup> David H. Weinberg,<sup>1,2,3</sup> Fiorenzo Vincenzo,<sup>1,2</sup> Jonathan C. Bird,<sup>4</sup> and Emily J. Griffith<sup>1</sup>

<sup>1</sup> Department of Astronomy, The Ohio State University, 140 W. 18th Ave., Columbus, OH, 43210, USA

<sup>2</sup> Center for Cosmology and Astroparticle Physics (CCAPP), The Ohio State University, 191 W. Woodruff Ave., Columbus, OH, 43210, USA

<sup>3</sup> Institute for Advanced Study, 1 Einstein Dr., Princeton, NJ, 08540, USA

<sup>4</sup> Department of Physics & Astronomy, Vanderbilt University, 2301 Vanderbilt Place, Nashville, TN, 37235, USA

Accepted XXX; Received YYY; in original form ZZZ

## ABSTRACT

We use a multi-ring galactic chemical evolution model to probe the astrophysical production of nitrogen (N) in the Milky Way. This approach treats individual annuli in the Galaxy disc as a conventional one-zone model, and to include the effects of radial migration, stellar populations move between annuli in a manner informed by star particles from a hydrodynamical simulation. We find that no published set of AGB star yields is able to reproduce the gas-phase [N/O]-[O/H] relation as observed; those that reproduce the qualitative trend still require an artificial enhancement of their N yields by factors of 2 – 3 to get the normalization correct. We demonstrate that, with a viable set of AGB star yields, our model is able to reproduce many of the observed correlations between N, O, and Fe abundances for stars when the N abundances are corrected for internal mixing processes within stars. With any of these yields, N production timescales are sufficiently short such that stellar migration is only a minimal source of intrinsic scatter in the observed [N/O]-[O/H] relation. Modest variations in the star formation rate and star formation efficiency produce considerably larger variations in the gas phase N and O abundances, consistent with previous observational arguments. Our models run using the publicly available **Versatile Integrator for Chemical Evolution** (VICE; <https://pypi.org/project/vice>). **To do: Play around with models with no metallicity dependence and no time dependence on the AGB N yields.**

**Key words:** methods: numerical – galaxies: abundances, evolution, star formation, stellar content

## 1 INTRODUCTION

• In terms of astrophysical nucleosynthesis, nitrogen (N) is a unique element.

– It’s one of only a few elements lighter than strontium ( $Z = 38$ ) with significant nucleosynthetic yields from asymptotic giant branch (AGB) stars (Johnson 2019).

– Alongside helium, it is one of the primary nuclear fusion products of main sequence stars more massive than the sun with nonzero metallicity. The CNO cycle catalyses the proton-proton chain of nuclear reactions (e.g. Suliga, Shalgar & Fuller 2020) using carbon (C), N, and oxygen (O) target nuclei,<sup>1</sup> the slowest component of which is the  $^{14}\text{N}(p,\gamma)^{15}\text{O}$  reaction. This bottleneck is strong enough that to first order, the effect of the CNO cycle is to convert all C and O isotopes in a star into  $^{14}\text{N}$ .

– It’s among a select group of elements whose observed abundances in stellar spectra often do not reflect the star’s birth abundances. The effect of internal mixing processes changes the atmospheric composition of red giants, a phenomenon both expected from theoretical models and observed in open and globular clusters (Gilroy 1989; Korn et al. 2007; Lind et al. 2008; Souto et al. 2018, 2019).

• Both observationally and theoretically, N is among the more well studied elements. Fig. 1 presents a compilation of observed abundances of N and O in the gas phase:

– HII regions in nearby NGC spirals (Pilyugin et al. 2010)

- HII regions in blue, diffuse star forming dwarf galaxies (Berg et al. 2012; Izotov et al. 2012; James et al. 2015)
- Local stars and HII regions (Dopita et al. 2016)
- Galactic and extragalactic HII regions (Henry et al. 2000)
- Star-forming regions in 550 nearby galaxies in the MaNGA IFU survey (Belfiore et al. 2017)

Despite intrinsic scatter and some systematic variation in how the abundances are determined, the [N/O]-[O/H] relation is more or less the same across a wide range of physical environments.

• In this paper, we’re interested in the origin of both the shape and scatter in this trend.

• N is not unique in that perhaps the largest source of uncertainty in modeling its abundances is that accurate and precise nucleosynthetic yields remain elusive. Presently, no combination of core collapse supernova explosion model and black hole landscape has been able to reproduce the observed abundance pattern of the elements, and nitrogen is no exception (Griffith et al. 2021). Furthermore, theoretical models of AGB stars predict different N yields as a function of progenitor mass and metallicity (see discussion in, e.g. § 5 of Karakas & Lugaro 2016 comparing their models to that of Cristallo et al. 2011, 2015).

• In this paper, we aim to constrain N yields from AGB stars empirically by assessing their ability to reproduce the observed abundance correlations between N and O, such as that illustrated in Fig. 1. Vincenzo et al. (2021) demonstrate that when N abundances are corrected for internal mixing processes, the correlations with stellar age and other elemental abundances are affected; whether or not these estimates of the birth abundances can be reproduced in galactic chemical evolution (GCE) models is also of central interest to this paper.

\* Contact e-mail: [johnson.7419@osu.edu](mailto:johnson.7419@osu.edu)

<sup>1</sup>  $^{12}\text{C}(p,\gamma)^{13}\text{N}(\beta^+,\nu_e)^{13}\text{C}(p,\gamma)^{14}\text{N}(p,\gamma)^{15}\text{O}(\beta^+,\nu_e)^{15}\text{N}(p,\alpha)^{12}\text{C}$

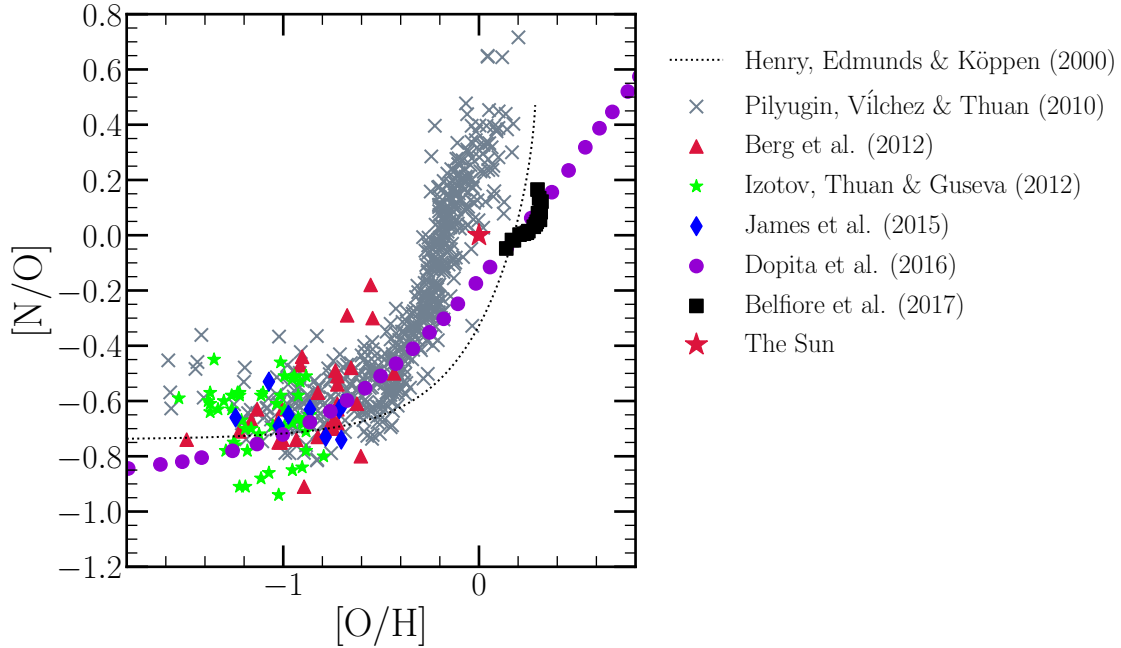


**Figure 1.** The  $[N/O]$ - $[O/H]$  relation observed in HII regions in nearby NGC spiral galaxies (grey X's: Pilyugin, Vílchez & Thuan 2010), in HII regions in blue, diffuse star forming dwarf galaxies (red triangles: Berg et al. 2012; green stars: Izotov, Thuan & Guseva 2012; blue diamonds: James et al. 2015), in local stars and HII regions (purple circles: Dopita et al. 2016), and in the MaNGA IFU survey (black squares: Belfiore et al. 2017). The fit to  $[N/O]$  as a function of  $[O/H]$  in Galactic and extragalactic HII regions by Henry, Edmunds & Köppen (2000) is shown in a black dotted line. The Sun, at (0, 0) on this plot by definition, is marked by a red star. We omit the uncertainties for visual clarity. **To do: Pull the data for CHAOS galaxies from Danielle Berg's and Noah Rogers's papers and add them to this figure.**

- In a sample of 6,507 galaxies from the Mapping Galaxies at Apache Point Observatory survey (MaNGA; Bundy et al. 2015), Schaefer et al. (2020) recently argued that intrinsic scatter in the  $[N/O]$ - $[O/H]$  relation is a consequence of variations in the local star formation efficiency. In regions of slower star formation, the  $[N/O]$  ratio tends to be slightly higher at fixed  $[O/H]$  (see their Fig. 4), as expected from GCE models (e.g. Mollá et al. 2006; Vincenzo et al. 2016). However, Schaefer et al. (2020) could not rule out radial migration as an additional source of scatter in the gas phase  $[N/O]$ - $[O/H]$  relation. Investigating GCE models for O and iron (Fe) abundances in the Milky Way which track the positions of stars as they migrate within the disc, Johnson et al. (2021) found that the characteristic delay time of type Ia supernovae (SNe Ia) is sufficiently long such that stellar migration has a noticeable impact on the Fe abundance in the ISM at a given Galactocentric radius and time. Since N is produced in significant quantities by AGB stars, which like SNe Ia are delayed nucleosynthetic sources, it's possible that its gas phase abundance could be affected by a deficit or surplus of AGB stars induced by radial migration; in a sufficiently large sample of galaxies like MaNGA this would present observationally as scatter in the gas phase abundances. The question of whether one of radial migration or star formation efficiency dominates over the other in driving this scatter is also of central interest in this paper.

## 2 METHODS: THE MULTI-ZONE CHEMICAL EVOLUTION MODEL

- Since we wish to test the impact of various assumptions about nucleosynthetic yields while taking into account stellar migration, multi-zone chemical evolution models are the ideal experiments. This allows us not only to entertain different assumptions regarding nucleosynthetic yields of N, but also affords us the ability to enforce a specific star formation history as well as slight variations to any of these assumptions - all within a framework that includes the impact of radial migration.

- We make use of the Milky Way models of Johnson et al. (2021), who originally constructed the model to explore the impact

of stellar migration on the observed abundances of O and Fe. This model makes use of the **Versatile Integrator for Chemical Evolution (VICE; Johnson & Weinberg 2020; Griffith et al. 2021; Johnson et al. 2021)**, an open-source python package for Unix system architectures. Because VICE recognizes most elements on the periodic table, computing N abundances with this model is easy. Though we provide a brief summary here, a full breakdown of the Johnson et al. (2021) model can be found in their § 2.

- As in previous models for the Milky Way (e.g. Matteucci & Francois 1989; Schönrich & Binney 2009; Minchev et al. 2013, 2014, 2017; Sharma et al. 2020), this model parameterizes the Galaxy disc as a series of concentric rings of width  $\delta R_{\text{gal}} = 100$  pc. Each ring is assigned its own star formation history (SFH), and with assumptions about the  $\Sigma_{\text{gas}} - \dot{\Sigma}_{\star}$  relation and outflows (see discussion below), VICE calculates the implied amounts of gas and infall at each timestep automatically. Each ring is assumed to be described by a conventional one-zone model of chemical evolution under the caveat that stellar populations can move between rings, which Johnson et al. (2021) demonstrate has a significant impact on the enrichment rates of delayed sources such as SNe Ia.

- To drive stellar migration, the model makes use of star particles from a hydrodynamical simulation, for which Johnson et al. (2021) chose the h277 galaxy from the Christensen et al. (2012) suite evolved with the N-body+SPH code GASOLINE (Wadsley et al. 2004); we retain this decision here. Previous studies have shown that h277, among other disc galaxies evolved with similar physics, has a realistic rotation curve (Governato et al. 2012; Christensen et al. 2014a,b), stellar mass (Munshi et al. 2013), metallicity (Christensen et al. 2016), dwarf satellite population (Zolotov et al. 2012; Brooks & Zolotov 2014), HI properties (Brooks et al. 2017), and age-velocity relation (Bird et al. 2021).

- Despite this, there are some interesting differences between h277 and the Milky Way. The last major merger in h277 was at a redshift of  $z \approx 3$ , making it an interesting case study for its quiescent merger history (e.g. Zolotov et al. 2012). The Milky Way is also known to have a strong, long-lived bar (e.g. Bovy et al. 2019), while h277 had only a weak and transient bar, lacking one at the present day.

- Radial migration proceeds from the h277 star particles in a simple manner; for a stellar population in our model born at a radius  $R_{\text{gal}}$  and a time  $T$ , VICE searches for star particles born at  $R_{\text{gal}} \pm 250$  pc and  $T \pm 250$  Myr. From the star particles that pass this cut, it then randomly selects one to act as that stellar population's *analogue*. The stellar population then assumes the present day midplane distance  $z$  and the change in orbital radius  $\Delta R_{\text{gal}}$  of its analogue. In the Johnson et al. (2021) fiducial model, stellar populations move to their implied final radii with a  $\sqrt{\text{age}}$  dependence, similar to the assumption made by Frankel et al. (2018, 2019). While they investigate the impact of this assumption, in the present paper we make use of only this model and one in which stellar migration is ignored. If VICE does not find any star particles from h277 in its initial search, it widens it to  $R_{\text{gal}} \pm 500$  pc and  $T \pm 500$  Myr; if still no candidate analogues are found, VICE maintains the  $T \pm 500$  Myr requirement, but assigns the star particle with the smallest difference in birth radius as the analogue. As in Johnson et al. (2021), these models neglect the impact of radial gas flows (e.g. Lacey & Fall 1985; Bilitewski & Schönrich 2012; Vincenzo & Kobayashi 2020), instead focusing on the impact of stellar migration.

- Although this model does impose some small but nonzero level of star formation at early times in the outer disc, the sample of star particles from h277 is sufficiently large that stellar populations that form there are typically assigned analogues which formed within  $\sim 2$  kpc of their birth radius. While ignoring effects such as the radial growth of the Galaxy (e.g. Bird, Kazantzidis & Weinberg 2012; Bird et al. 2013), this at least ensures that these old, outer disc populations are assigned stellar populations which give them an outer disc rather than an inner disc dynamical history.

- Rather than using a hydrodynamical simulation, some previous studies have implemented stellar migration using dynamical arguments (e.g. Schönrich & Binney 2009; Sharma et al. 2020).

- An advantage of our approach over this is that these dynamical arguments introduce free parameters into the model which then require fitting to data. A disadvantage is that we are restricted to one realization of our dynamical history; slight variations are not possible.

- This model does not distinguish between “blurring” and “churning”, terms often used to refer to the epicyclic motions of stars and changes in their guiding centres, respectively. These effects are induced by a variety of physical interactions such as molecular cloud scattering (Mihalas & Binney 1981; Jenkins & Binney 1990; Jenkins 1992), orbital resonances with spiral arms or bars (Sellwood & Binney 2002; Minchev et al. 2011), and satellite perturbations (Bird et al. 2012); both are present in h277.

- Our fiducial model here has the same SFH as that of Johnson et al. (2021), where the time-dependence at a given  $R_{\text{gal}}$  is given by:

$$f(t|R_{\text{gal}}) = (1 - e^{-t/\tau_{\text{rise}}})e^{-t/\tau_{\text{sff}}}, \quad (1)$$

where  $\tau_{\text{rise}}$  approximately controls the amount of time the SFR is rising at early times; we set this parameter equal to 2 Gyr at all radii as in Johnson et al. (2021). Our e-folding timescales  $\tau_{\text{sff}}$  are taken from a fit of this functional form to the  $\Sigma_{\star}$ -age relation in bins of  $R/R_{\text{e}}$  for  $10^{10.5} - 10^{11} M_{\odot}$  Sa/Sb Hubble type spiral galaxies reported by Sánchez (2020). The resulting values of  $\tau_{\text{sff}}$  are long:  $\sim 15$  Gyr at the solar circle ( $R_{\text{gal}} = 8$  kpc) and as high as  $\sim 40$  Gyr in the outer disc (see their Fig. 3), which is primarily a consequence of the flat nature of the  $\Sigma_{\star}$ -age relation reported by Sánchez (2020).

- Within each  $\delta R_{\text{gal}} = 100$  pc ring, the normalization of the SFH is set by the total stellar mass of the Milky Way disc and the present-day surface density gradient assuming it is unaffected by stellar migration (see Appendix B of Johnson et al. 2021). For the former, we neglect the contribution from the bulge and adopt the total disc stellar mass of  $5.17 \times 10^{10} M_{\odot}$  from Licquia & Newman (2015). For the latter, we adopt a double exponential form describing the separate thin- and thick-disc components. We take the scale radii of the thin- and thick-discs to be  $R_t = 2.5$  kpc and  $R_T = 2.0$  kpc with a surface density ratio

at  $R_{\text{gal}} = 0$  of  $\Sigma_T/\Sigma_t = 0.27$  based on the findings of Bland-Hawthorn & Gerhard (2016).

- The Johnson et al. (2021) models run VICE in star formation mode, meaning that the user specifies the SFH and the amount of gas and infall at each timestep are calculated automatically by the code. Determining the gas supply requires an assumption about the star formation law (often referred to as “star formation efficiency” in the chemical evolution literature, though this term has other meanings in, e.g., the star formation and feedback community). Previously, GCE models have adopted a single power-law relating  $\Sigma_{\text{gas}}$  and  $\dot{\Sigma}_{\star}$  based on the findings of Kennicutt (1998), but recent studies have revealed that the star formation law on a galaxy-by-galaxy basis is much more nuanced (de los Reyes & Kennicutt 2019; Ellison et al. 2021; Kennicutt & de los Reyes 2021), and some of the uncertainty regarding its details can be traced back to the ongoing debate about the CO-to-H<sub>2</sub> conversion factor (Kennicutt & Evans 2012; Liu, Gao & Greve 2015). Based on a compilation of the Bigiel et al. (2010) and Leroy et al. (2013) data shown in comparison to the theoretically motivated star formation laws of Krumholz et al. (2018, see their Fig. 2), Johnson et al. (2021) take a three-component power-law as their star formation law with the index given by:

$$N = \begin{cases} 1.0 & (\Sigma_{\text{gas}} \geq 2 \times 10^7 M_{\odot} \text{ kpc}^{-2}) \\ 3.6 & (5 \times 10^6 M_{\odot} \text{ kpc}^{-2} \leq \Sigma_{\text{gas}} \leq 2 \times 10^7 M_{\odot} \text{ kpc}^{-2}) \\ 1.7 & (\Sigma_{\text{gas}} \leq 5 \times 10^6 M_{\odot} \text{ kpc}^{-2}). \end{cases} \quad (2)$$

The normalization of the star formation law is then set by letting the SFE timescale  $\tau_{\star} \equiv \Sigma_{\text{gas}}/\dot{\Sigma}_{\star}$  be given by the value derived observationally for molecular gas at surface densities where  $N = 1$ . The value of  $\tau_{\star}$  for molecular gas at the present day is taken to be  $\tau_{\text{mol},0} = 2$  Gyr (Leroy et al. 2008, 2013) with a  $t^{1/2}$  time-dependence based on the findings of Tacconi et al. (2018) studying the  $\Sigma_{\text{gas}} - \dot{\Sigma}_{\star}$  relation as a function of redshift.

- Because of the yields adopted in the Johnson et al. (2021) models, considerable outflows are required in order to predict plausible abundances. Weinberg et al. (2017) demonstrate analytically that to first order the equilibrium abundance of some element in the ISM is determined by its yield and the mass-loading factor  $\eta = \dot{\Sigma}_{\text{out}}/\dot{\Sigma}_{\star}$  with a small correction for the SFH. Johnson et al. (2021) make use of this to select a scaling of  $\eta$  with  $R_{\text{gal}}$  such that the equilibrium abundance as a function of radius corresponds to a reasonable metallicity gradient within the Galaxy (see their Fig. 3 and discussion in § 3.1).

### 3 NUCLEOSYNTHESIS

- Although we’re computing abundances for N, O, and Fe in the present paper, O and Fe were already explored in detail by Johnson et al. (2021), and we retain their parameterization of O and Fe supernova yields here. The supernova yields are defined as the net mass of some element X produced over all supernova events in units of the progenitor star cluster’s mass. For example, with a yield of  $y_X = 0.001$ , a  $1000 M_{\odot}$  cluster would produce  $1 M_{\odot}$  of the element X instantaneously in the case of CCSNe and over the delay time distribution (DTD) in the case of SNe Ia. We take the following values from Johnson et al. (2021), who in turn base them off of Weinberg et al. (2017) and Johnson & Weinberg (2020):

$$\begin{aligned} - y_{\text{O}}^{\text{CC}} &= 0.015 \\ - y_{\text{Fe}}^{\text{CC}} &= 0.0012 \\ - y_{\text{O}}^{\text{Ia}} &= 0 \\ - y_{\text{Fe}}^{\text{Ia}} &= 0.00214 \end{aligned}$$

- We set  $y_{\text{N}}^{\text{Ia}}$  to zero and spend the remainder of this section detailing our CCSN and AGB star yields of N.

#### 3.1 Core Collapse Supernovae

- In VICE, CCSN nucleosynthetic products are approximated to be produced instantaneously following an episode of star formation;

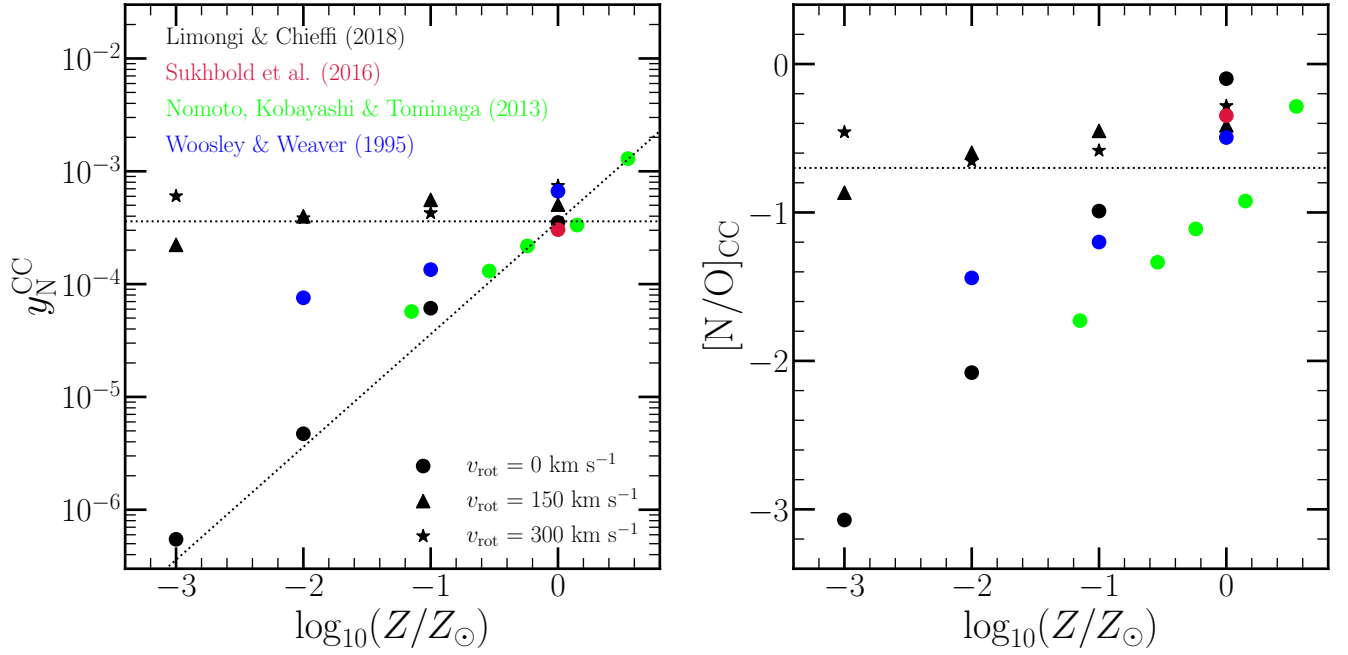


**Figure 2.** **Left:** IMF-averaged CCSN yields of N calculated using VICE’s `vice.yields.ccsne.fractional` function with the tables published by Woosley & Weaver (1995, blue), Nomoto, Kobayashi & Tominaga (2013, green), Sukhbold et al. (2016, red), and Limongi & Chieffi (2018, black). All studies report yields for non-rotating progenitors only with the exception of Limongi & Chieffi (2018), who also report yields for progenitor rotational velocities of 150 (triangles) and 300 km/s (stars). **Right:** The  $[N/O]$  ratio predicted by each of the explosion models in the left-hand panel, under the same colour-coding and marker scheme. We mark the position of  $[N/O] = -0.7$  with a black dotted line, the value roughly suggested by the observations of low-metallicity systems highlighted in Fig. 1.

this is a valid approximation due to how short the lives of massive stars are compared to the relevant timescales for GCE. The yield is the constant of proportionality between the CCSN production rate and the SFR:

$$\dot{M}_X^{CC} = y_X^{CC} \dot{M}_\star. \quad (3)$$

- At low  $[O/H]$ <sup>1</sup>, the mean  $[N/O]$  is near  $\sim -0.7$  (see Fig. 1). Since the AGB star yields of N are believed to increase with metallicity (e.g., C11+C15; V13), this is likely the regime in which N yields are dominated by CCSN enrichment. We therefore take  $[N/O]_{cc} \approx -0.7$  empirically.

- Based on the definition of the abundance ratio  $[X/Y]$ , we can relate the CCSN yields of N and O to one another given this result:

$$[N/O]_{cc} = \log_{10} \left( \frac{y_N^{CC}}{y_O^{CC}} \right) - \log_{10} \left( \frac{Z_{N,\odot}}{Z_{O,\odot}} \right) \quad (4a)$$

$$y_N^{CC} = y_O^{CC} 10^{[N/O]_{cc}} \left( \frac{Z_{N,\odot}}{Z_{O,\odot}} \right), \quad (4b)$$

where  $Z_{X,\odot}$  is the abundance by mass of some element X in the sun.

- Taking  $Z_{N,\odot} = 6.91 \times 10^{-4}$  and  $Z_{O,\odot} = 5.7 \times 10^{-3}$  based on the solar photospheric abundances of Asplund et al. (2009) and our value of  $y_O^{CC} = 0.015$  yields  $y_N^{CC} = 3.6 \times 10^{-4}$ , which we adopt as our fiducial CCSN yield of N. We mark this value with a horizontal dotted line in the left hand panel of Fig. 2. We discuss the sloped dotted line in that panel in the context of some of our AGB star yield models in § 4.2.

- Can we understand this value with theoretically predicted N yields? To address this, we compute IMF-averaged net yields of N using VICE’s `vice.yields.ccsne.fractional` function assuming a Kroupa (2001) IMF; for details, we refer readers to § 4 of Griffith et al. (2021) and the VICE science documentation.<sup>2</sup> The left panel of Fig. 2 plots the results as a function of progenitor metallicity predicted

by the Woosley & Weaver (1995), Nomoto et al. (2013), Sukhbold et al. (2016), and Limongi & Chieffi (2018) tables.

- Only Limongi & Chieffi (2018) report yields for progenitors with a non-zero rotational velocity, and these are the only values consistent with  $y_N^{CC} = 3.6 \times 10^{-4}$  at low metallicity. For non-rotating progenitors, every study investigated here can reproduce approximately this value at solar metallicity only, with the predictions at lower Z falling short of the empirical value, in some cases by orders of magnitude.

- It is unsurprising that  $y_N^{CC}$  is so dependent on the rotational velocity at low metallicity.  $y_N^{CC}$  is itself highly uncertain at low Z (Heger & Woosley 2010), but most of the N production in CCSN progenitors occurs via the CNO cycle processing C and O isotopes into  $^{14}N$ . With few C and O seed nuclei at low Z, production of  $^{14}N$  is difficult. Rotationally induced mixing, also a highly uncertain process (Zahn 1992; Maeder & Zahn 1998; Lagarde et al. 2012), could transport newly produced C and O into the hydrogen burning shell of the CCSN progenitor, facilitating N production (Frischknecht et al. 2016; see also discussion in § 4.2 of Andrews et al. 2017). For this reason, N yields at low metallicity are highly sensitive to the assumptions about mixing.

- In the right-hand panel of Fig. 2, we make use of equation (4a) to compare the  $[N/O]$  ratios predicted by these studies; the horizontal black dashed line denotes  $[N/O]_{cc} = -0.07$ , the empirical value taken from Fig. 1. The fact that the points follow similar trends between the two panels is a consequence of the fact that these studies predict relatively metallicity-independent O yields.

- Again, only the rotating models of Limongi & Chieffi (2018) are able to reproduce this value at low metallicity. At solar metallicity the supernova models predict a higher  $[N/O]_{cc}$ , but our value of  $[N/O]_{cc}$  is taken at low metallicity, so that is the most relevant comparison.

### 3.2 Asymptotic Giant Branch Stars

- In the present paper, we’re interested in the question of how well the “off the shelf” AGB star yield models for N can reproduce the observed  $[N/O]$ - $[O/H]$  relation.

- [As discussed in § 1,] the majority of nitrogen production occurs through the CNO cycle, the slowest component of which is

<sup>1</sup> We follow the standard notation where  $[X/Y] \equiv \log_{10}(X/Y) - \log_{10}(X/Y)_\odot$ .

<sup>2</sup> [https://vice-astro.readthedocs.io/en/latest/science\\_documentation/yields/index.html](https://vice-astro.readthedocs.io/en/latest/science_documentation/yields/index.html)



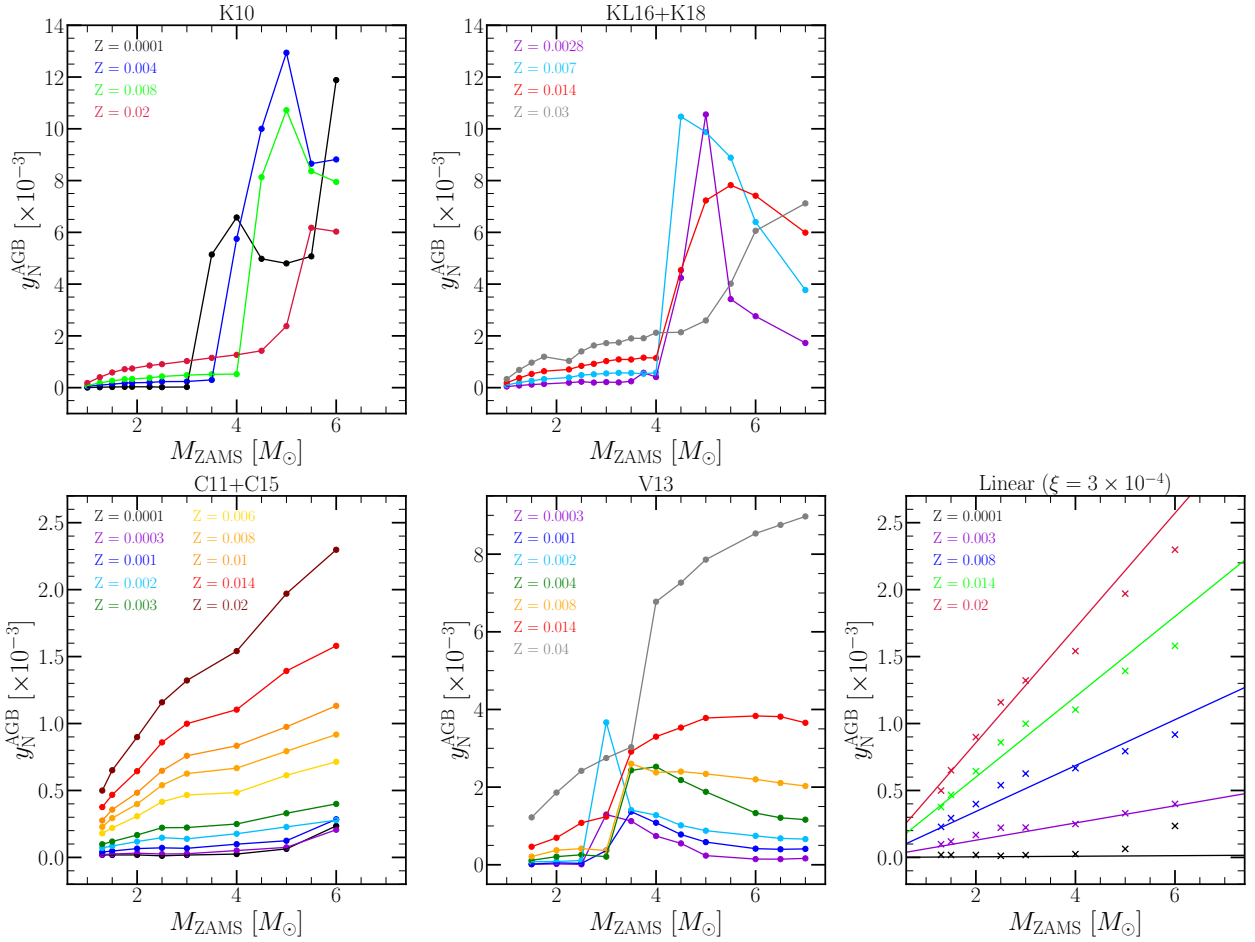


**Figure 3.** The fractional yields of N from AGB stars  $y_N^{\text{AGB}}$  as a function of progenitor ZAMS mass and birth metallicity  $Z$  as reported by Karakas (2010) (upper left), Karakas & Lugaro (2016) and Karakas et al. (2018) (upper middle), Cristallo et al. (2011, 2015) (lower left), and Ventura et al. (2013) (lower middle). In the lower right panel, we show the yields predicted by our linear model (colored lines; see discussion in § X) in comparison to the Cristallo et al. (2011, 2015) predictions (colored X's).

the  $^{14}\text{N}(\text{p},\gamma)^{15}\text{O}$  reaction which produces a bottleneck, effectively turning all of the different C, N, and O isotopes into  $^{14}\text{N}$ .

- Similar to the SN yields (see discussion above), these are defined as fractional net yields in that they quantify only the newly produced N in the AGB star ejecta in units of its ZAMS mass. For a yield  $y_N^{\text{AGB}}(M_\star, Z_\star)$ , the actual mass yield is then given by  $M_\star y_N^{\text{AGB}}(M_\star, Z_\star)$ . AGB star enrichment proceeds as it does in Johnson & Weinberg (2020) under the caveat that the yield is placed in the  $\delta R_{\text{gal}} = 100$  pc ring that a stellar population is in at a given time. In short, VICE implements an algorithm which calculates the mass in dying stars from each previous star formation event (i.e. timestep), and the ZAMS mass required to calculate the yield comes from a mass-lifetime relation (e.g. Hurley, Pols & Tout 2000).

- In the present paper, we make use of four previously published yields calculated from stellar evolution models on a table of progenitor masses and metallicities. Two of these yield sets are already built in VICE:

- The default set of yields is published in Cristallo et al. (2011, 2015) (hereafter C11+C15). We illustrate these yields as a function of ZAMS mass for the available metallicities in the lower left panel of Fig. 3. This is the most comprehensive set of yields in VICE in that it includes tables for all elements built into the code and is sampled at the most metallicities.
- The Karakas (2010, hereafter K10) is plotted in the upper left panel of Fig. 3.

With this paper we build in the following additional sets of AGB star yield tables:

- The Ventura et al. (2013, hereafter V13) yields are illustrated in the bottom middle panel of Fig. 3.
- We combine the yields published in Karakas & Lugaro (2016) at  $Z = 0.007, 0.014$ , and  $0.03$  with those published in Karakas et al. (2018) at  $Z = 0.0028$ ; we hereafter refer to these tables as the KL16+K18 set of yields. We plot them in the upper middle panel of Fig. 3.

- VICE also allows users to construct their own functions of progenitor mass and metallicity to describe the AGB star yield. As an additional test, we construct a model in which the yield is linearly proportional to both progenitor ZAMS mass and metallicity according to:

$$y_N^{\text{AGB}} = \xi \left( \frac{M}{M_\odot} \right) \left( \frac{Z}{Z_\odot} \right) \quad (5)$$

We illustrate this model in the lower right panel of Fig. 3 for  $\xi = 3 \times 10^{-4}$ . We compare this model to the C11+C15 yields by including the colored X's on this panel. In general, the two yield models agree rather well.

- Despite reporting values of the same physical quantities, the N yields reported by each of these studies show substantial differences between one another. Unfortunately, a direct comparison between AGB star yield tables is difficult, because each study employs different assumptions for mass loss, convection and convective boundaries within the star, and nuclear reaction networks, all of which have a significant impact on stellar evolution and consequently the predicted abundances. However, the two most important physical processes in determining AGB star yields of all the CNO species is third dredge up (TDU) and hot bottom burning (HBB), and some of the differences

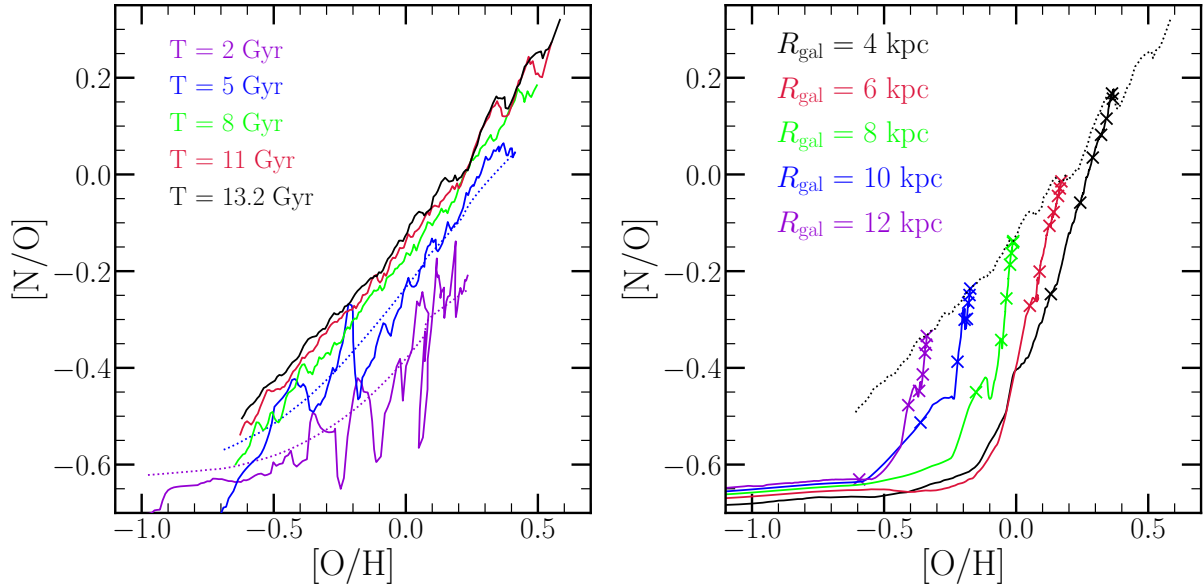


**Figure 4.** **Left:** The gas-phase  $[N/O]$ - $[O/H]$  relation parameterized by radius at various snapshots (solid coloured lines) in our fiducial model with the **C11+C15** yields. Dotted lines denote the resulting relation at  $T = 2$  and  $5$  Gyr in the model where we neglect stellar migration. **Right:** The gas-phase  $[N/O]$ - $[O/H]$  relation parameterized by time at fixed radius (solid coloured lines) in the fiducial model. X's denote the abundances at  $T = 2, 4, 6, 8, 10, 12$ , and  $13.2$  Gyr (the present day) at these radii. The dotted line is the same as the solid black line in the left hand panel.

between these yield sets can be understood through the interaction between the two.

- TDU refers to the repeated penetrations of the convective envelope into the hydrogen depleted core during the thermal pulses associated with AGB star evolution. This process doesn't affect N abundances much, but replenishes the outer layers of the star with C and O. In low mass AGB stars, the main source of free neutrons is the  $^{13}\text{C}(\alpha, n)^{16}\text{O}$  reaction, which can occur at substantial rates when C is mixed with the He-rich shell during each TDU episode.

- HBB refers to the activation of proton captures at the base of the convective envelope, which activates the CNO cycle, producing large amounts of  $^{14}\text{N}$  at the expense of C and O. HBB requires a higher mass AGB star progenitor ( $\sim 4 - 5 M_{\odot}$  at  $Z_{\odot}$ ) than TDU ( $\sim 2 - 2.5 M_{\odot}$  at  $Z_{\odot}$ ), but the minimum mass for both decreases at lower metallicity.

- The most efficient N production occurs when both TDU and HBB occur within an AGB star, because each replenishment of C and O isotopes from the core adds new seed nuclei for the CNO cycle when HBB is active. This is the reason for the substantial N production above  $\sim 4 M_{\odot}$  in the **K10** and **KL16+K18** models; in both yield sets, every star that experiences HBB also experiences TDU. Both TDU and HBB are more efficient at low metallicity (see discussion in **V13**). In the case of TDU, each penetration of the convective envelope into the H-depleted core is deeper because of the lower opacity. For HBB, the base of the convective envelope is hotter, increasing the rate of nuclear reactions relative to the higher  $Z$  models. Though there are some exceptions evident in Fig. 3, as a consequence the highest N yields in the **K10** and **KL16+K18** models are for low metallicity stars above  $\sim 4 M_{\odot}$ .

- This interaction between TDU and HBB is also the reason for the increase in N yields in the **V13** tables near  $\sim 3 M_{\odot}$ . Unlike the **K10** and **KL16+K18** models, their stars experience both TDU and HBB only in this narrow range in mass.

- Of all of these yields taken from the literature, the **C11+C15** sample shows the smoothest dependence on progenitor mass and metallicity. Unfortunately, ascertaining the exact cause of this difference between the other yields explored here is difficult; relative to the **KL16+K18** yields (see discussion in their § 5), the **C11+C15** models have more mass loss, a  $\sim 10\%$  faster triple- $\alpha$  reaction rate, weaker HBB, and fewer thermal pulses overall. Though their agreement is good below  $\lesssim 3 M_{\odot}$ , the fact that

HBB is weaker and fewer TDU episodes are experienced does however lend a qualitative explanation into why the **C11+C15** yields are so much smaller than the **K10** and **KL16+K18** yields at higher masses.

- In the interest of consistency, when we adopt a particular AGB star yield model for N, we also adopt it for O and Fe. However, the AGB star yields of these elements are negligible compared to their supernova yields.

## 4 RESULTS

### 4.1 The Fiducial Model

- Our fiducial model adopts, together with the supernova yields of **Johnson et al. (2021)**, see discussion in § 2),  $y_{\text{N}}^{\text{CC}} = 3.6 \times 10^{-4}$  and the **C11+C15** AGB star yield tables.

- To obtain the  $[N/O]$ - $[O/H]$  relation predicted by the model, we simply take the N and O abundances in the gas-phase at a given time for each  $\delta R_{\text{gal}} = 100$  pc ring at  $R_{\text{gal}} > 2$  kpc and plot them as a line. We show the results at five output times in the left hand panel of Fig. 4. The relation is generally time-independent after  $T \gtrsim 5$  Gyr, though there is some evolution toward higher  $[N/O]$ .

- The small bumpy features in the relation are caused by stellar migration; in comparison, the dotted lines plotted at  $T = 2$  and  $5$  Gyr quantify the prediction when migration is neglected (i.e. the “post-processing” model from **Johnson et al. 2021**). At a given time, the movements of stars between rings induce a slight surplus or deficit in the number of AGB stars enriching some annulus. This is similar to what **Johnson et al. (2021)** found for SN Ia enrichment of Fe (see discussion in their §§ 3.2 and 3.4). Generally the effect is small for N ( $< 0.1$  dex), but there are some instances at early times where the impact of stellar migration is more substantial.

- In our models, the  $[N/O]$ - $[O/H]$  relation arises as a superposition of endpoints rather than an evolutionary phase. We demonstrate this in the middle panel of Fig. 4, where we plot the time-evolution of  $[N/O]$  and  $[O/H]$  at  $R_{\text{gal}} = 4, 6, 8, 10$ , and  $12$  kpc in relation to the predicted  $[N/O]$ - $[O/H]$  relation at the present day. Rather than each annulus's track passing through some well-defined region of this parameter space, they instead each evolve upward more or less parallel to one another. The result is an  $[N/O]$ - $[O/H]$  relation that reflects the Galaxy's metallicity gradient more so than different evolutionary

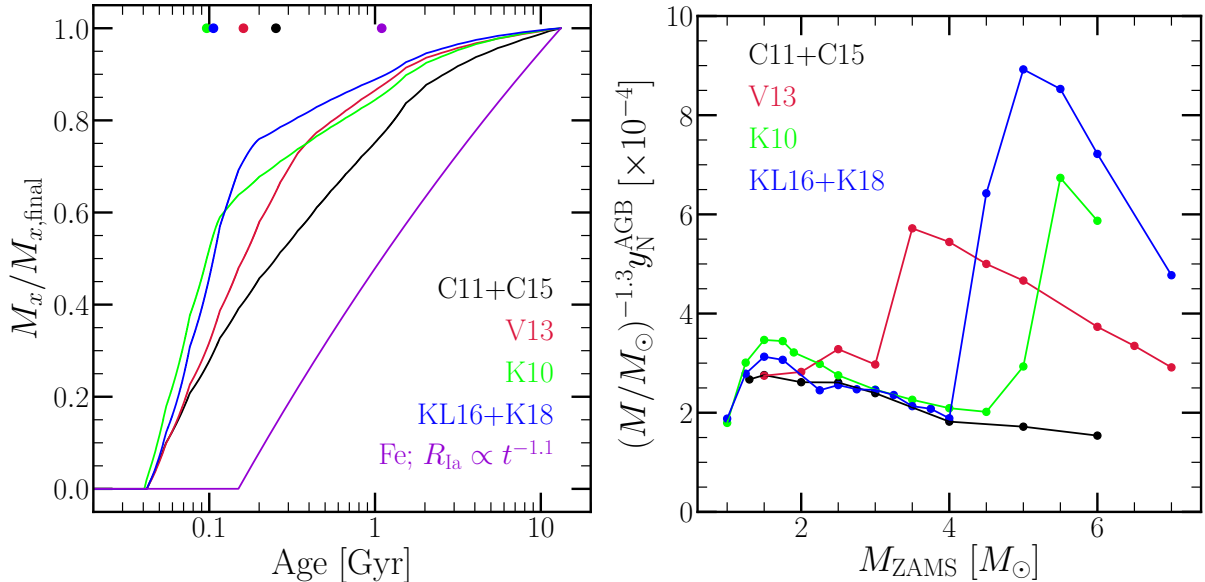


**Figure 5.** **Left:** The net mass of N produced by AGB stars from a single stellar population for each of our yield models at solar metallicity ( $Z = 0.02$  in **K10**,  $Z = 0.014$  otherwise). The purple line denotes the same for Fe assuming our  $t^{-1.1}$  delay time distribution. All values are normalized to the total mass produced at an age of 13.2 Gyr. Points at the top of the panel denote the ages at which 50% of the total mass yield has been produced. **Right:** The IMF-weighted mass yield of N from AGB stars as a function of progenitor mass at the same metallicities as in the left panel.

states. Similar arguments have been made regarding the low  $[\alpha/\text{Fe}]$  stars in the Galaxy (see, e.g., Schönrich & Binney 2009; Sharma et al. 2020).

#### 4.2 Alternate Yield Models

- The smaller impact of stellar migration on N than Fe abundances can be understood by their timescales for production from single stellar populations. To demonstrate this, we make use of VICE’s `vice.single_stellar_population` function, which computes the mass yield of a given element as a function of time from a star cluster of known metallicity. For the sake of this calculation, we set  $y_{\text{N}}^{\text{CC}}$  and  $y_{\text{Fe}}^{\text{CC}}$  both to zero in order to highlight only the delayed nucleosynthetic sources. We plot the results of this procedure in the left panel of Fig. 5 for each of our AGB star yield models at solar metallicity ( $Z = 0.02$  for **K10**,  $Z = 0.014$  otherwise). Under our fiducial model, it takes  $\sim 250$  Myr for a single stellar population to produce  $\sim 50\%$  of its N from AGB stars. For Fe, this characteristic delay time is near  $\sim 1$  Gyr, an order of magnitude larger.<sup>1</sup> Johnson et al. (2021) find that the Fe enrichment rate can vary by as much as a factor of  $\sim 3$  due only to stellar migration (see their Fig. 8 and discussion in their § 3.4). This is largely because the timescales for migration are comparable to the timescales for SN Ia explosions, but the same is not true for N. Instead, N is produced on shorter timescales, meaning that single stellar populations generally eject most of their yield to the ISM before their orbits can change significantly.

- Despite minor differences in the details of the predicted delay time distributions, there is good qualitative agreement between our different AGB star yield models. Our fiducial model with **C11+C15** yields is the slowest, owing to the larger N production in  $\gtrsim 3 M_{\odot}$  stars in the alternate models. As a consequence, the alternate models predict even less variability in the gas phase N abundances due to stellar migration.

- In the right hand panel of Fig. 5, we plot the IMF-weighted mass yield of nitrogen for each of our yield models at the same metallicities as in the left hand panel. Since our yields are fractional (or rather, in

units of the progenitor star’s mass; see discussion in § 3.2), the mass yield is given by  $M y_{\text{N}}^{\text{AGB}}$ . With an additional weight of  $M^{-2.3}$  from the IMF in this mass range (Kroupa 2001), we thus multiply each yield by  $(M/M_{\odot})^{-1.3}$ . Compared to the fiducial model, the contribution of higher mass AGB stars to the total N production is quite substantial. The difference can be understood by the interaction between TDU and HBB discussed in § 3.2 which effects the evolution of stars at these masses.

- The left hand panel of Fig. 6 compares the predictions of our model made with each of the AGB star yield models discussed in § 3.2 and visualized in Fig. 3. For observational reference, we include the Dopita et al. (2016) measurements also plotted in Fig. 1.

- In order to successfully reproduce the observations, we find that we need to artificially amplify the **C11+C15** and **V13** yields by factors of  $\sim 3$  and  $\sim 2$ , respectively. Having originally comparing our linear model to the **C11+C15** yields in Fig. 3 with  $\xi = 3 \times 10^{-4}$ , we amplify the value of  $\xi$  by a factor of 3 here as well. Although these models predict an  $[\text{N/O}]-[\text{O/H}]$  relation that is slightly shallower than the Dopita et al. (2016) measurements, the predictions are reasonably within the scatter seen in Fig. 1. **To do: Alternatively, can this be explained by a lowering of the O yields and  $\eta$ , or a differential wind which preferentially removes oxygen (Vincenzo et al. 2016)?**

- We are unable to reproduce the observed trend with either the **K10** or **KL16+K18** yield models.

- In the case of **K10**, the model overpredicts  $[\text{N/O}]$  at low  $[\text{O/H}]$  and predicts  $[\text{N/O}]$  to *decrease* monotonically with increasing  $[\text{O/H}]$ . With a slope of the wrong sign, there is no multiplicative factor by which we can amplify or suppress these yields in order to reproduce the observations.

- The **KL16+K18** yields improve upon the **K10** predictions to some extent. The overprediction of  $[\text{N/O}]$  at low  $[\text{O/H}]$  is largely corrected, but it predicts a relatively flat trend of  $[\text{N/O}]$  above  $[\text{O/H}] \gtrsim -0.2$ , leading still to an underprediction of  $[\text{N/O}]$  at high  $[\text{O/H}]$ .

- Can an alternate parameterization of  $y_{\text{N}}^{\text{CC}}$  reproduce the observations with the **K10** and **KL16+K18** AGB star yield models?

- If the **K10** yields are to reproduce the observations, the overall N abundance must decrease at low  $[\text{O/H}]$  and increase at high  $[\text{O/H}]$ ; one way to do this is with a metallicity-dependent CCSN yield. We therefore construct the following parameteriza-

<sup>1</sup> This is exactly as expected with a  $\sim t^{-1}$  DTD as adopted in Johnson et al. (2021). Half of the SNe Ia occur between 100 Myr and 1 Gyr, and the other half between 1 and 10 Gyr.

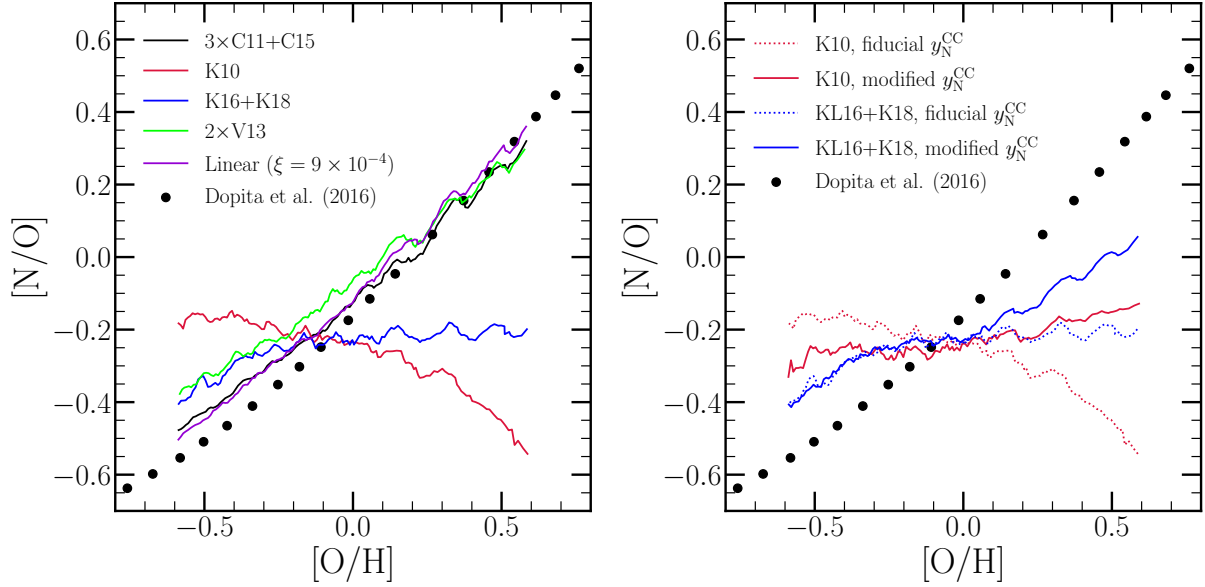


**Figure 6.** **Left:** The present day gas-phase  $[N/O]$ - $[O/H]$  relation predicted by our fiducial model with each of the yield sets described in § 3.2. The **C11+C15** and **V13** yields are artificially amplified by factors of 3 and 2, respectively, and we take the linear model with  $\xi = 9 \times 10^{-4}$ . For observational reference, we plot the population-averaged trend for local stars and HII regions reported by [Dopita et al. \(2016\)](#). **Right:** The same as the left-hand panel, but comparing the predictions made by the **K10** and **KL16+K18** yields with our fiducial value of  $y_N^{CC}$  (dotted lines, same as left-hand panel) to those with the alternate forms of  $y_N^{CC}$  (solid lines) given by equation X for the **K10** yields and equation Y for the **KL16+K18** yields.

tion of  $y_N^{CC}$ :

$$y_N^{CC} = (3.6 \times 10^{-4}) \left( \frac{Z}{Z_\odot} \right). \quad (6)$$

We illustrate this model with the slanted black dotted in Fig. 2. While our fiducial model best describes the rotating CCSN models of [Limongi & Chieffi \(2018\)](#), this alternate parameterization better characterizes the non-rotating models of [Limongi & Chieffi \(2018\)](#), [Sukhbold et al. \(2016\)](#), [Nomoto et al. \(2013\)](#), and [Woosley & Weaver \(1995\)](#) while maintaining the same base-line value of  $3.6 \times 10^{-4}$  at solar metallicity.

- If the **KL16+K18** yields are to reproduce the observed results, then contrary to the predictions made with the **K10** yields, the overall N abundance at low  $[O/H]$  is fine. Instead, it's only the N abundance at high  $[O/H]$  that needs correcting. We therefore construct a second alternate form of  $y_N^{CC}$  by retaining the value of the fiducial yield at sub-solar metallicity but assuming the value of equation (6) above solar metallicity:

$$y_N^{CC} = \begin{cases} 3.6 \times 10^{-4} & (Z \leq Z_\odot) \\ (3.6 \times 10^{-4}) \left( \frac{Z}{Z_\odot} \right) & (Z \geq Z_\odot). \end{cases} \quad (7)$$

- We compare our model predictions with these alternate CCSN yields for the **K10** and **KL16+K18** AGB star yields in the right hand panel of Fig. 6. These modifications were able to make up some of the difference, but both models still predict an  $[N/O]$ - $[O/H]$  relation that is simply too shallow to explain the observations. Although we cannot reproduce the data with either the **K10** or **KL16+K18** yield models, they suffer from similar issues as the **C11+C15** and **V13** yields.

- The underprediction of N yields at high metallicity is not unique to **K10** and **KL16+K18**; we have to amplify the **C11+C15** and **V13** yields by factors of a few for this exact reason.

- At low  $[O/H]$ , the **KL16+K18** yields are actually the only ones that can explain the observed N abundances without any modification. The **K10** yields, however, overpredict the N abundances at low metallicity.

- The inverse dependence of  $[N/O]$  with  $[O/H]$  when taking the **K10** yields can be understood by the interaction between

TDU and HBB (see discussion in § 3.2). Both effects are stronger at low metallicity, and since all of the **K10** models experiencing HBB also experience TDU (see their Table 1), such a result is not surprising. This is also true for the **KL16+K18** yields, but that model predicts a relatively flat  $[N/O]$ - $[O/H]$  relation.

- We cannot say with any confidence based on our GCE models whether or not such a wide mass range of stars should experience both TDU and HBB. On the one hand, this makes it difficult for the model to predict a monotonic increase in  $[N/O]$  with increasing  $[O/H]$ . On the other hand, such strong N production at low metallicity in the **KL16+K18** yields is what allows them to explain the N abundances at low  $[O/H]$  with no modification.

- We believe these results are independent of the choice of the CCSN yield of O  $y_O^{CC}$ . Our value of  $y_O^{CC} = 0.015$  is based on models in which all stars with a ZAMS mass above  $8 M_\odot$  explode as a CCSN (e.g. [Chieffi & Limongi 2013](#)), but the [Johnson et al. \(2021\)](#) models assume substantial outflows such that the equilibrium abundance corresponds to a reasonable metallicity gradient within the Galaxy. If we were to lower all of our CCSN yields by a factor of 3 to account for failed supernovae (e.g. [Sukhbold et al. 2016](#)), then we would have to also lower our mass loading factors by a factor of 3 to predict similar overall abundances ([Weinberg et al. 2017](#)). Our model would thus compute similar AGB star yields for N in such a scenario.

### 4.3 The Stellar Abundances

- Before comparing the predictions of GCE models to observational data, it is essential that the N abundances be adjusted to account for internal processes that alter the surface compositions of stars. This is an important step to take before comparing GCE models to observational data, because GCE models predict the birth abundances of stars, and N abundances in evolved stars do not reflect their birth abundance. After the CNO cycle has processed much of the C and O nuclei into  $^{14}\text{N}$  during a star's main sequence lifetime, this N-rich material from the core is mixed with the outer convective layers, increasing the N abundance in the photosphere. Using MESA stellar evolution models ([Paxton et al. 2011, 2013, 2015, 2018](#)) with standard



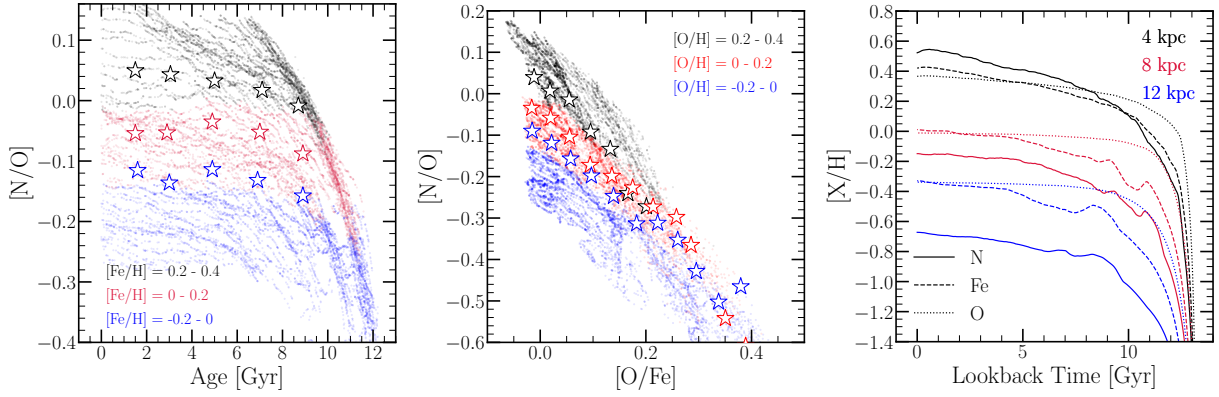


**Figure 7.** **Left:** [N/O] as a function of stellar age for 5000 stars randomly sampled from our model stellar populations in three bins of [Fe/H] (colored points). Stars quantify the median trend of [N/O] with age corrected for internal mixing in the same bins of [Fe/H] from the Vincenzo et al. (2021) sample. **Middle:** The same as the left hand panel, instead showing [N/O] as a function of [O/Fe] in bins of [O/H]. **Right:** [N/O] (solid), [Fe/H] (dashed), and [O/H] (dotted) in the gas phase as a function of lookback time at  $R_{\text{gal}} = 4$  (black), 8 (red), and 12 kpc (blue).

mixing prescriptions, Vincenzo et al. (2021) developed a prescription to approximate the birth abundances of C, N, and O and apply it to a sample of APOGEE/Kepler red giants.

- In the left hand panel of Fig. 7, we compare our model predictions to their [N/O] abundances with the ages taken from Miglio et al. (2021). The model correctly predicts that the [N/O]-age relation is relatively flat in bins of [Fe/H]. This is an important success of the model, because with uncorrected N abundances, [N/O] vs. age exhibits a significant negative slope at fixed [Fe/H] (see Fig. 7 of Vincenzo et al. 2021). Our model does, however, slightly under-predict [N/O] in the [Fe/H] =  $-0.2 - 0$  bin. In general, our model occupies a wider range in [N/O] at all ages than does the Vincenzo et al. (2021) measurements, suggesting that our yields scale with metallicity slightly too strongly.

- In the middle panel of Fig. 7, we compare our model predicted [N/O]-[O/Fe] relation to their calculations. As in the left hand panel, our model predicted stellar populations occupy a wider range of [N/O] than the data, but the agreement is otherwise good. The model correctly predicts that [N/O] should increase with decreasing [O/Fe] at all metallicities, and places the increase in [N/O] in the highest [O/H] bin at approximately the correct value of [O/Fe].

- These results can generally be understood with the notion that N and Fe abundances change on similar timescales in our model. In the right hand panel of Fig. 7, we show the time evolution of [N/H], [Fe/H], and [O/H] in the gas phase at three different radii. [N/H] is more correlated with [Fe/H] than [O/H] at all radii, and the relation persists up to lookback times of  $\sim 10$  Gyr. This arises largely because N and Fe are both produced in different quantities by delayed enrichment sources while O is produced almost entirely on short timescales by CCSNe (see discussion in § 3). As a consequence of its single dominant nucleosynthetic source, O reaches an equilibrium abundance on much shorter timescales than elements like N and Fe which have significant contributions from delayed sources (Weinberg et al. 2017); because of this, [O/H] is nearly independent of lookback time as far back as  $\sim 10$  Gyr ago while [N/H] and [Fe/H] are not. Therefore, a bin in [Fe/H] is also approximately a bin in [N/H], and with [O/H] more or less constant, the [N/O]-age relation at fixed [Fe/H] is relatively flat up to ages of  $\sim 10$  Gyr. The anti-correlation between [N/O] and [O/Fe] at fixed [O/H] is also a direct consequence of the N-Fe correlation.

- We thus conclude that when a viable model for the AGB star yields of N is adopted, our GCE models are in good agreement with observed abundances of N when corrected for internal mixing processes known to affect the photospheric abundances in red giant stars.

#### 4.4 The Sources of Scatter in the [N/O]-[O/H] Relation

- What is the dominant source of variance in the observed [N/O]-[O/H] relation? Schaefer et al. (2020) demonstrate that intrinsic scatter is driven by variations in the local SFE - with slower star formation, more AGB stars enrich the ISM by the time it reaches a given abundance, causing a higher [N/O] at fixed [O/H]. However, they did not rule out radial migration as another source of scatter. Can the radial migration of nucleosynthetic yields drive enough variation in the gas-phase [N/O]-[O/H] relation to explain these results too? Our models, taking into account the effects of radial migration on the enrichment rates, are the ideal tool with which to answer this question.

- We construct two additional models based on our fiducial model, one in which the SFE exhibits 25% sinusoidal variations in time, and the other with the same 25% variations in the SFR. In these models, the SFE timescale  $\tau_{\star}$  and SFH  $\dot{\Sigma}_{\star}$  are modified from the fiducial case in the following manner:

$$\tau_{\star}(R_{\text{gal}}, t) = \tau_{\star, \text{J21}}(R_{\text{gal}}, t) \left( 1 + 0.25 \sin \left( \frac{2\pi t}{2 \text{ Gyr}} \right) \right) \quad (8)$$

$$\dot{\Sigma}_{\star}(R_{\text{gal}}, t) = \dot{\Sigma}_{\star, \text{J21}}(R_{\text{gal}}, t) \left( 1 + 0.25 \sin \left( \frac{2\pi t}{2 \text{ Gyr}} \right) \right), \quad (9)$$

where  $\tau_{\star, \text{J21}}$  and  $\dot{\Sigma}_{\star, \text{J21}}$  refer to the SFE timescale and SFH in the fiducial model taken from Johnson et al. (2021).

- In a real galaxy, the variability in the SFE and the SFR are likely non-sinusoidal and not with constant amplitude. This, however, at least quantifies how much variation in [N/O] can be expected by variations of a fixed amplitude in these quantities.

- We find that 25% variations in these quantities generally induce larger variability than does stellar migration. In the left hand panel of Fig. 8, we plot the predicted gas-phase [N/O]-[O/H] relation at high [O/H] for five snapshots covering one cycle of the fluctuations induced by variability in  $\tau_{\star}$ . The model with no sinusoidal oscillations in  $\tau_{\star}$  predicts the relation to be nearly constant over this time interval, whereas the model with them predicts a  $\sim 0.15$ -dex dynamic range.

- Such behavior is driven by the constant tug-of-war between dilution and re-enrichment associated with oscillations in  $\tau_{\star}$ . In this model,  $\dot{\Sigma}_{\star}$  is the same as it was in Johnson et al. (2021), so it is not  $\dot{\Sigma}_{\star}$  which is fluctuating, but rather  $\Sigma_{\text{gas}}$ . When the gas supply increases, the ISM becomes diluted, decreasing [O/H]. Because the AGB star yields of N with our fiducial C11+C15 model are roughly linear with metallicity, the decrease in the N abundance due to the now lowered yields are in direct proportion to the amount of dilution. As a result, [N/O] is only marginally affected by the fluctuations in the overall abundance. The variations in the [N/O]-[O/H] relation that the model predicts are therefore more of a consequence of variability in [O/H] than in [N/O]. We demonstrate this with the black dashed line in the left hand panel of Fig. 8, which traces out the evolution of the

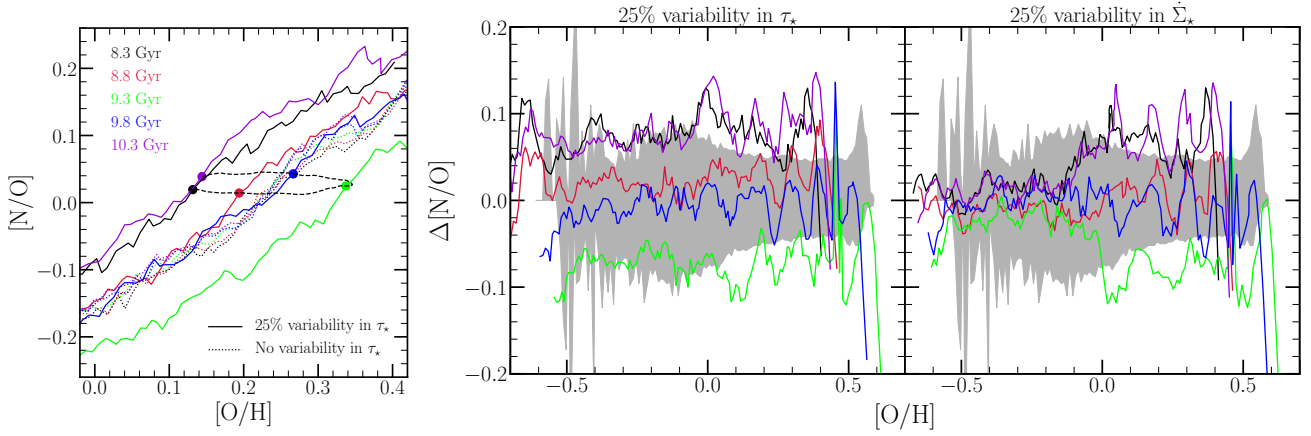


**Figure 8.** **Left:** One cycle of oscillations in the  $[N/O]$ - $[O/H]$  relation at high  $[O/H]$  induced by 25% sinusoidal variability in  $\tau_\star$  (solid coloured lines). Dotted lines show the  $[N/O]$ - $[O/H]$  relation at the same five snapshots in the fiducial model with no variability in  $\tau_\star$ . The black dashed line shows the time evolution of the abundances in the  $R_{\text{gal}} = 5$  kpc ring, with the times of each of the five snapshots marked by a coloured point. **Middle and Right:** For the same five snapshots in the left hand panel, the deviation in  $[N/O]$  at fixed  $[O/H]$  relative to the fiducial model for the case with 25% variability in  $\tau_\star$  (middle) and in  $\Sigma_\star$  (right). The shaded regions in both panels quantify the width of the  $[N/O]$  distribution in  $10^{10.5} - 10^{11} M_\odot$  galaxies in MaNGA taken from [Schaefer et al. \(2020\)](#). The median  $[N/O]$  is placed at  $\Delta[N/O] = 0$ , and the lower (upper) envelope denotes the 16th (84th) percentile of the  $[N/O]$  distribution at a given  $[O/H]$ .

abundances at  $R_{\text{gal}} = 5$  kpc over the same time interval. In general,  $[N/O]$  is affected only at the  $\sim 0.05$ -dex level while  $[O/H]$  varies with an amplitude of  $\sim 0.25$ -dex. As the gas supply falls off, enrichment proceeds in a gas-starved ISM, which increases  $[O/H]$  once more, but  $[N/O]$  to a lesser extent for similar reasons, and the cycle repeats itself.

- When  $\Sigma_\star$  varies,  $\Sigma_{\text{gas}}$  and consequently the abundances vary instead at a value of  $\tau_\star$  that varies only as much as the adopted  $\Sigma_\star - \Sigma_{\text{gas}}$  relation from [Johnson et al. \(2021\)](#) dictates it should (see discussion in § 2), with no additional variations in time.

- In the middle and right hand panels of Fig. 8, we plot the difference in  $[N/O]$  at fixed  $[O/H]$  between the fiducial model and those with variability as a function of  $[O/H]$  (i.e. the vertical offset between the solid and dotted curves in the left hand panel). Both scenarios produce offsets in  $[N/O]$  at high  $[O/H]$  (which as discussed above are truly offsets in  $[O/H]$  at fixed  $[N/O]$ ), but the model with variations in  $\Sigma_\star$  does not predict any significant fluctuations in the abundances at  $[O/H] \lesssim -0.2$ . This is a consequence of the mathematical form of  $\tau_{\star, \text{J21}}$  (see discussion in § 2) and the fact that we have run these models in star formation mode with VICE. The low  $[O/H]$  end of the relation comes from the outer Galaxy at lower  $\Sigma_{\text{gas}}$  than the inner regions at higher  $[O/H]$ , and the surface densities are in the region where  $\Sigma_{\text{gas}} \sim \Sigma_\star^{3.6}$ . However, in these models,  $\Sigma_\star$  is fixed, meaning that it is not a strong function of  $\Sigma_{\text{gas}}$  - rather  $\Sigma_{\text{gas}}$  is only a weak function of  $\Sigma_\star$ . 25% oscillations in  $\Sigma_\star$  therefore have little impact on the ISM gas supply, and as a consequence the impact on abundances is minimal. At smaller  $R_{\text{gal}}$  (i.e. higher  $[O/H]$ ),  $\Sigma_{\text{gas}}$  varies more strongly with  $\Sigma_\star$ , and thus there is a stronger effect on the abundances there. In the model with oscillations in  $\tau_\star$ ,  $\Sigma_{\text{gas}}$  always varies with a 25% amplitude, so the oscillations are seen at all abundances. If we were to adopt an alternate form of the  $\Sigma_\star - \Sigma_{\text{gas}}$  relation in these models, such as a purely linear or single power-law formalism, then the impact on abundance would be seen at all  $[O/H]$  when  $\Sigma_\star$  oscillates. Alternatively, we expect a similar result if we were to run an equivalent model in infall mode (i.e. specifying the infall history and initial gas supply rather than the star formation history).

- The shaded regions in the left and middle panels of Fig. 8 quantify the scatter in the gas-phase  $[N/O]$ - $[O/H]$  relation inferred observationally by [Schaefer et al. \(2020\)](#). Using data from Mapping nearby Galaxies at Apache Point Observatory (MaNGA; [Bundy et al. 2015](#)), an integral field unit survey, they measure N and O abundances in 709,541 spaxels across 6,507 unique galaxies spanning a stellar mass range from  $10^9 - 10^{11} M_\odot$ . Since our model is appropriate for Milky Way mass galaxies, we focus our comparison on the  $M_\star = 10^{10.5} - 10^{11} M_\odot$  range, which cuts our sample to 197,787

individual N and O measurements from the MaNGA IFU spaxels. In narrow bins of  $[O/H]$ , we then compute the median  $[N/O]$  as well as the 16th and 84th percentiles of the  $[N/O]$  distribution. Placing the median  $[N/O]$  at  $\Delta[N/O] = 0$ , the shaded regions above and below 0 in Fig. 8 denote the difference between the 16th and 84th percentile of the distribution in each bin.

- Our models with 25% sinusoidal oscillations in  $\Sigma_\star$  and  $\tau_\star$  produce deviations in  $[N/O]$  at fixed  $[O/H]$  that are comparable to the width of the distribution measured observationally. Stellar migration, on the other hand, induces only small variations, as can be seen in the left-hand panel of Fig. 8. This traces back to the timescales of N production from single stellar populations (see Fig. 6 and discussion in § 4.1): most N production occurs quickly following a stellar population's formation ( $\sim$ few hundred Myr), meaning that most stars will not migrate far from their birth radius by the time they produce their N, and the resulting impact on the gas phase abundances is minimal.

- In general, galaxies will not have perfectly sinusoidal variations in their SFR or SFE, and they will also not be of a constant amplitude. Nonetheless, these models clearly demonstrate that the expected differences in N and O abundances in the gas phase is larger than that caused by radial migration as conjectured by [Schaefer et al. \(2020\)](#). Such variations will present as scatter in the gas phase abundances by observing many galaxies at different phases and with different amplitudes in their variability, which may be much more complicated than the sinusoids modeled here.

## 5 CONCLUSIONS

- We have made use of the GCE models from [Johnson et al. \(2021\)](#) which characterize the Milky Way disc as a series of concentric rings with a uniform  $\delta R_{\text{gal}} = 100$  pc width. These models treat each individual ring as a conventional one-zone model of chemical evolution while allowing individual stellar populations to move between rings to include the effects of stellar migration.

- If we assume the IMF-averaged CCSN yield of O from [Johnson et al. \(2021\)](#) ( $y_{\text{O}}^{\text{CC}} = 0.015$ ), we find that the CCSN models with rotating progenitors from [Limongi & Chieffi \(2018\)](#) are able to reproduce the N yield inferred empirically from the “plateau” at  $[N/O] \approx -0.7$  at low  $[O/H]$  (see Fig. 1;  $y_{\text{N}}^{\text{CC}} = 3.6 \times 10^{-4}$ ). The non-rotating models, on the other hand, fall short of this value at low metallicities. Instead taking the values of  $y_{\text{O}}^{\text{CC}}$  inferred from the [Limongi & Chieffi \(2018\)](#) yields, we find that their rotating models are also able to reproduce  $[N/O]_{\text{cc}} = -0.7$  at low metallicities, with the non-rotating models again falling short of this value.

- We find that there are substantial differences between the mass-

and metallicity-dependencies of the AGB star yields of N (see Fig. 3). Although a one-to-one comparison is difficult because each model folds in different assumptions about, e.g., mass loss, convection and convective boundaries, and nuclear reactions networks, the differences can largely be understood by the interaction between TDU and HBB in the model AGB stars.

- We find that in the absence of a starburst event, the gas phase [N/O]-[O/H] relation is relatively time-independent up to lookback times of  $\sim 6 - 8$  Gyr in our fiducial model. Similar to arguments that have been made regarding the low-[ $\alpha$ /Fe] population in the Milky Way (e.g. Schönrich & Binney 2009; Sharma et al. 2020; Johnson et al. 2021), we find that the [N/O]-[O/H] relation arises not out of an evolutionary sequence but as a superposition of endpoints of multiple evolutionary sequences. That is, the time evolution of each ring through the [N/O]-[O/H] plane is not the same line as the [N/O]-[O/H] relation that would be observed at the present day in our model Galaxy (see Fig. 6).

- We find that the timescales for N production by a single stellar population ( $\sim 100$  Myr) are considerably shorter than that of Fe production in our models ( $\sim 1$  Gyr). As a consequence, most N production occurs before a stellar population's orbit will change significantly, and stellar migration has only a minimal impact on the gas phase [N/O]-[O/H] relation. Because the timescales for Fe production are longer, Johnson et al. (2021) find that the impact on the enrichment rates is significant, and may be enough to explain the presence of young,  $\alpha$ -rich stars in the solar neighbourhood as seen in APOGEE (Chiappini et al. 2015; Martig et al. 2015, 2016; Jofré et al. 2016; Yong et al. 2016; Izzard et al. 2018; Silva Aguirre et al. 2018; Warfield et al. 2021). This difference underscores the argument from Johnson et al. (2021) that in order for nucleosynthetic yields to migrate along with their progenitor stellar populations, the characteristic delay time for the production of some element must be comparable to the timescales of stellar migration.

- We find that no single AGB star yield model previously published in the literature is able to reproduce the gas-phase [N/O]-[O/H] relation as observed. Our fiducial model with the C11+C15 yields requires an artificial amplification by a factor of  $\sim 3$  in order to get the normalization correct. We find similar results with the V13 yields (factor of  $\sim 2$  amplification). The K10 yields predict [N/O] to decrease with increasing [O/H]: a slope with the wrong sign. Although the KL16+K18 yields predict a flat [N/O]-[O/H] relation, they're able to explain the N abundances at low [O/H]; this is the only previously published yield model in this paper that is able to explain the N abundances at any metallicity. Even with alternate forms for our CCSN yields as suggested by the non-rotating models of Woosley & Weaver (1995), Nomoto et al. (2013), Sukhbold et al. (2016), and Limongi & Chieffi (2018), our model is able to reproduce the observed [N/O]-[O/H] relation with neither the K10 nor the KL16+K18 yield models.

- We find that our model is able to reproduce the correlations of [N/O] with [O/Fe] and stellar age when N abundances are corrected for internal mixing processes in stars. Vincenzo et al. (2021) found that even after these corrections were made, the N abundances of thin- and thick-disc stars persisted; our model is able to reproduce this result. Vincenzo et al. (2021) also found the [N/O]-age relation in bins of [Fe/H] to be flat, whereas with uncorrected N abundances there is a significant negative slope. In agreement with Vincenzo et al. (2021), our model predicts the [N/O]-age relation to be flat when a selection in [Fe/H] is made. Both of these predictions trace back to our model predicting N abundances to increase in the ISM at a similar rate as Fe out to lookback times  $\lesssim 8$  Gyr. Because of this, a range in [Fe/H] maps approximately to a range in [N/O], and as a result, [N/O] increases as [O/Fe] decreases.

- We find that 25% sinusoidal oscillations in the SFR and SFE induce larger variability in the [N/O]-[O/H] relation than does stellar migration. In detail, the fluctuations are mostly in [O/H] rather than in [N/O], and this presents as a higher [N/O] at fixed [O/H], but our models suggest a slightly more accurate statement is to characterize these fluctuations as higher or lower [O/H] at fixed [N/O] (see discussion in § 4.4). We find that these models can accurately explain

the intrinsic scatter in the gas phase [N/O]-[O/H] relation as inferred observationally by Schaefer et al. (2020), consistent with their argument and supporting their conjecture that radial migration is not the dominant source of scatter in their data. Although real galaxies likely have neither perfectly sinusoidal variations in their SFR or SFE nor with a constant amplitude, these models demonstrate clearly that such variability induces fluctuations in the gas phase N and O abundances larger than that caused by stellar migration.

- The results outlined in this paper highlight the importance of empirically calibrated yields of all elements from all nucleosynthetic sources in GCE models. The combination of theoretically predicted yields with flexible computational tools such as VICE can provide powerful constraints for future models of stellar evolution and element production.

## 6 ACKNOWLEDGEMENTS

We acknowledge valuable discussion with Jennifer Johnson, Adam Leroy, Grace Olivier, Amy Sardone, Jiayi Sun, Todd Thompson, and other members of The Ohio State Astronomy Gas, Galaxies, and Feedback group. This work was supported by National Science Foundation grant AST-1909841. D.H.W. is grateful for the hospitality of the Institute for Advanced Study and the support of the W.M. Keck Foundation and the Hendricks Foundation. F.V. acknowledges the support of a Fellowship from the Center for Cosmology and Astroparticle Physics at The Ohio State University.

## REFERENCES

- Andrews B. H., Weinberg D. H., Schönrich R., Johnson J. A., 2017, *ApJ*, **835**, 224
- Asplund M., Grevesse N., Sauval A. J., Scott P., 2009, *ARA&A*, **47**, 481
- Belfiore F., et al., 2017, *MNRAS*, **469**, 151
- Berg D. A., et al., 2012, *ApJ*, **754**, 98
- Bigiel F., Leroy A., Walter F., Blitz L., Brinks E., de Blok W. J. G., Madore B., 2010, *AJ*, **140**, 1194
- Bilitewski T., Schönrich R., 2012, *MNRAS*, **426**, 2266
- Bird J. C., Kazantzidis S., Weinberg D. H., 2012, *MNRAS*, **420**, 913
- Bird J. C., Kazantzidis S., Weinberg D. H., Guedes J., Callegari S., Mayer L., Madau P., 2013, *ApJ*, **773**, 43
- Bird J. C., Loebman S. R., Weinberg D. H., Brooks A. M., Quinn T. R., Christensen C. R., 2021, *MNRAS*, **503**, 1815
- Bland-Hawthorn J., Gerhard O., 2016, *ARA&A*, **54**, 529
- Bovy J., Leung H. W., Hunt J. A. S., Mackereth J. T., García-Hernández D. A., Roman-Lopes A., 2019, *MNRAS*, **490**, 4740
- Brooks A. M., Zolotov A., 2014, *ApJ*, **786**, 87
- Brooks A. M., Papastergis E., Christensen C. R., Governato F., Stilp A., Quinn T. R., Wadsley J., 2017, *ApJ*, **850**, 97
- Bundy K., et al., 2015, *ApJ*, **798**, 7
- Chiappini C., et al., 2015, *A&A*, **576**, L12
- Chieffi A., Limongi M., 2013, *ApJ*, **764**, 21
- Christensen C., Quinn T., Governato F., Stilp A., Shen S., Wadsley J., 2012, *MNRAS*, **425**, 3058
- Christensen C. R., Brooks A. M., Fisher D. B., Governato F., McCleary J., Quinn T. R., Shen S., Wadsley J., 2014a, *MNRAS*, **440**, L51
- Christensen C. R., Governato F., Quinn T., Brooks A. M., Shen S., McCleary J., Fisher D. B., Wadsley J., 2014b, *MNRAS*, **440**, 2843
- Christensen C. R., Davé R., Governato F., Pontzen A., Brooks A., Munshi F., Quinn T., Wadsley J., 2016, *ApJ*, **824**, 57
- Cristallo S., et al., 2011, *ApJS*, **197**, 17
- Cristallo S., Straniero O., Piersanti L., Gobrecht D., 2015, *ApJS*, **219**, 40
- de los Reyes M. A. C., Kennicutt Robert C. J., 2019, *ApJ*, **872**, 16
- Dopita M. A., Kewley L. J., Sutherland R. S., Nicholls D. C., 2016, *Ap&SS*, **361**, 61
- Ellison S. L., Lin L., Thorp M. D., Pan H.-A., Scudder J. M., Sánchez S. F., Bluck A. F. L., Maiolino R., 2021, *MNRAS*, **501**, 4777
- Frankel N., Rix H.-W., Ting Y.-S., Ness M., Hogg D. W., 2018, *ApJ*, **865**, 96
- Frankel N., Sanders J., Rix H.-W., Ting Y.-S., Ness M., 2019, *ApJ*, **884**, 99
- Frischnecht U., et al., 2016, *MNRAS*, **456**, 1803
- Gilroy K. K., 1989, *ApJ*, **347**, 835
- Governato F., et al., 2012, *MNRAS*, **422**, 1231



- Griffith E. J., Sukhbold T., Weinberg D. H., Johnson J. A., Johnson J. W., Vincenzo F., 2021, arXiv e-prints, [p. arXiv:2103.09837](#)
- Heger A., Woosley S. E., 2010, *ApJ*, **724**, 341
- Henry R. B. C., Edmunds M. G., Köppen J., 2000, *ApJ*, **541**, 660
- Hurley J. R., Pols O. R., Tout C. A., 2000, *MNRAS*, **315**, 543
- Izotov Y. I., Thuan T. X., Guseva N. G., 2012, *A&A*, **546**, A122
- Izzard R. G., Preece H., Jofre P., Halabi G. M., Masseron T., Tout C. A., 2018, *MNRAS*, **473**, 2984
- James B. L., Kopolov S., Stark D. P., Belokurov V., Pettini M., Olszewski E. W., 2015, *MNRAS*, **448**, 2687
- Jenkins A., 1992, *MNRAS*, **257**, 620
- Jenkins A., Binney J., 1990, *MNRAS*, **245**, 305
- Jofré P., et al., 2016, *A&A*, **595**, A60
- Johnson J. A., 2019, *Science*, **363**, 474
- Johnson J. W., Weinberg D. H., 2020, *MNRAS*, **498**, 1364
- Johnson J. W., et al., 2021, arXiv e-prints, [p. arXiv:2103.09838](#)
- Karakas A. I., 2010, *MNRAS*, **403**, 1413
- Karakas A. I., Lugaro M., 2016, *ApJ*, **825**, 26
- Karakas A. I., Lugaro M., Carlos M., Cseh B., Kamath D., García-Hernández D. A., 2018, *MNRAS*, **477**, 421
- Kennicutt Robert C. J., 1998, *ApJ*, **498**, 541
- Kennicutt R. C., Evans N. J., 2012, *ARA&A*, **50**, 531
- Kennicutt Robert C. J., de los Reyes M. A. C., 2021, *ApJ*, **908**, 61
- Korn A. J., Grundahl F., Richard O., Mashonkina L., Barklem P. S., Collet R., Gustafsson B., Piskunov N., 2007, *ApJ*, **671**, 402
- Kroupa P., 2001, *MNRAS*, **322**, 231
- Krumholz M. R., Burkhardt B., Forbes J. C., Crocker R. M., 2018, *MNRAS*, **477**, 2716
- Lacey C. G., Fall S. M., 1985, *ApJ*, **290**, 154
- Lagarde N., Decressin T., Charbonnel C., Eggenberger P., Ekström S., Palacios A., 2012, *A&A*, **543**, A108
- Leroy A. K., Walter F., Brinks E., Bigiel F., de Blok W. J. G., Madore B., Thornley M. D., 2008, *AJ*, **136**, 2782
- Leroy A. K., et al., 2013, *AJ*, **146**, 19
- Licquia T. C., Newman J. A., 2015, *ApJ*, **806**, 96
- Limongi M., Chieffi A., 2018, *ApJS*, **237**, 13
- Lind K., Korn A. J., Barklem P. S., Grundahl F., 2008, *A&A*, **490**, 777
- Liu L., Gao Y., Greve T. R., 2015, *ApJ*, **805**, 31
- Maeder A., Zahn J.-P., 1998, *A&A*, **334**, 1000
- Martig M., et al., 2015, *MNRAS*, **451**, 2230
- Martig M., et al., 2016, *MNRAS*, **456**, 3655
- Matteucci F., Francois P., 1989, *MNRAS*, **239**, 885
- Miglio A., et al., 2021, *A&A*, **645**, A85
- Mihalas D., Binney J., 1981, Galactic astronomy. Structure and kinematics
- Minchev I., Famaey B., Combes F., Di Matteo P., Mouhcine M., Wozniak H., 2011, *A&A*, **527**, A147
- Minchev I., Chiappini C., Martig M., 2013, *A&A*, **558**, A9
- Minchev I., Chiappini C., Martig M., 2014, *A&A*, **572**, A92
- Minchev I., Steinmetz M., Chiappini C., Martig M., Anders F., Matijevic G., de Jong R. S., 2017, *ApJ*, **834**, 27
- Mollá M., Vílchez J. M., Gavilán M., Díaz A. I., 2006, *MNRAS*, **372**, 1069
- Munshi F., et al., 2013, *ApJ*, **766**, 56
- Nomoto K., Kobayashi C., Tominaga N., 2013, *ARA&A*, **51**, 457
- Paxton B., Bildsten L., Dotter A., Herwig F., Lesaffre P., Timmes F., 2011, *ApJS*, **192**, 3
- Paxton B., et al., 2013, *ApJS*, **208**, 4
- Paxton B., et al., 2015, *ApJS*, **220**, 15
- Paxton B., et al., 2018, *ApJS*, **234**, 34
- Pilyugin L. S., Vílchez J. M., Thuan T. X., 2010, *ApJ*, **720**, 1738
- Sánchez S. F., 2020, *ARA&A*, **58**, 99
- Schaefer A. L., Tremonti C., Belfiore F., Pace Z., Bershady M. A., Andrews B. H., Drory N., 2020, *ApJ*, **890**, L3
- Schönrich R., Binney J., 2009, *MNRAS*, **396**, 203
- Sellwood J. A., Binney J. J., 2002, *MNRAS*, **336**, 785
- Sharma S., Hayden M. R., Bland-Hawthorn J., 2020, arXiv e-prints, [p. arXiv:2005.03646](#)
- Silva Aguirre V., et al., 2018, *MNRAS*, **475**, 5487
- Souto D., et al., 2018, *ApJ*, **857**, 14
- Souto D., et al., 2019, *ApJ*, **874**, 97
- Sukhbold T., Ertl T., Woosley S. E., Brown J. M., Janka H. T., 2016, *ApJ*, **821**, 38
- Suliga A. M., Shalgar S., Fuller G. M., 2020, arXiv e-prints, [p. arXiv:2012.11620](#)
- Tacconi L. J., et al., 2018, *ApJ*, **853**, 179
- Ventura P., Di Criscienzo M., Carini R., D'Antona F., 2013, *MNRAS*, **431**, 3642
- Vincenzo F., Kobayashi C., 2020, *MNRAS*, **496**, 80
- Vincenzo F., Belfiore F., Maiolino R., Matteucci F., Ventura P., 2016, *MNRAS*, **458**, 3466
- Vincenzo F., et al., 2021, arXiv e-prints, [p. arXiv:2106.03912](#)
- Wadsley J. W., Stadel J., Quinn T., 2004, *New Astron.*, **9**, 137
- Warfield J. T., et al., 2021, *AJ*, **161**, 100
- Weinberg D. H., Andrews B. H., Freudenburg J., 2017, *ApJ*, **837**, 183
- Woosley S. E., Weaver T. A., 1995, *ApJS*, **101**, 181
- Yong D., et al., 2016, *MNRAS*, **459**, 487
- Zahn J. P., 1992, *A&A*, **265**, 115
- Zolotov A., et al., 2012, *ApJ*, **761**, 71